Corrosion Science 102 (2016) 209–221

Contents lists available at ScienceDirect

Corrosion Science

journal homepage: www.elsevier.com/locate/corsci

Corrosion resistance of dicalcium phosphate dihydrate/poly(lactic-co-glycolic acid) hybrid coating on AZ31 magnesium alloy

Xia Li[a], Zhengyang Weng[a], Wei Yuan[b], Xianzi Luo[a], Hoi Man Wong[c], Xiangmei Liu[a], Shuilin Wu[a,d,*], K.W.K. Yeung[c], Yufeng Zheng[b], Paul. K. Chu[d]

[a] Hubei Collaborative Innovation Center for Advanced Organic Chemical Materials, Ministry-of-Education Key Laboratory for the Green Preparation and Application of Functional Materials, Hubei Province Key Laboratory of Industrial Biotechnology, School of Materials Science & Engineering, Hubei University, Wuhan, China
[b] State Key Laboratory for Turbulence and Complex System and Department of Materials Science and Engineering, College of Engineering, Peking University, Beijing 100871, China
[c] Division of Spine Surgery, Department of Orthopaedics & Traumatology, Li Ka Shing Faculty of Medicine, The University of Hong Kong, Hong Kong, China
[d] Department of Physics & Materials Science, City University of Hong Kong, Tat Chee Avenue, Kowloon, Hong Kong, China

ARTICLE INFO

Article history:
Received 30 June 2015
Received in revised form 8 October 2015
Accepted 9 October 2015
Available online 19 October 2015

Keywords:
A. Alloy
A. Magnesium
B. EIS
C. Passive films

ABSTRACT

A hydrid coating composed of dicalcium phosphate dihydrate (DCPD) and poly(lactic-co-glycolic acid) (PLGA) is prepared on AZ31 Mg alloy to control the corrosion resistance. The DCPD coating is deposited on the AZ31 substrate by electrochemical deposition and subsequently covered by the PLGA coating. Potentiodynamic and electrochemical impedance spectroscopy (EIS) tests conducted in simulated body fluid at 37 °C indicate that the corrosion resistance of the AZ31 is improved significantly by this hybrid coating. The deposition time influences the morphology and structure of the DCPD coating and consequently affects the corrosion resistance of both the DCPD and DCPD/PLGA coated samples.

1. Introduction

Magnesium (Mg) and its alloys are attractive biomaterials in tissue reconstruction [1–5] due to their unique advantages over conventional biomaterials such as stainless steels, titanium alloys, and CoCr alloys including natural biodegradability [6,7], mechanical properties similar to those of natural bone [8,9], and biocompatibility [10,11]. In addition, Mg in the proper concentration range promotes the growth of new bone tissues [12,13]. Many types of Mg-based alloys such as Mg–Ca [14], Mg–Zn [15], Mg–Sr [16], Mg–Si [17] and Mg–Zr [18] have been developed and have clinical potential in screws for therapy of hallux valgus [19], and stents for vascular remodeling [20,21], as well as bone implants [22].

However, the degradation rates of Mg alloys tend to be quite high at pH of less than 11.5 [23] and the presence of chloride ions accelerates corrosion of Mg alloys in chloride-containing solutions such as the human body fluid or blood plasma [24]. Fast degradation leads to premature loss of mechanical integrity of the implants before tissues have adequate time to heal. In addition, rapid corrosion causes excessive secretion of lytic protein BMP which leads to the lytic phenomenon [25], and a large amount of hydrogen is generated to delay bone healing. The high local alkalinity may also induce inflammation and allergic reactions [26]. Therefore, it is crucial to control the corrosion rate of Mg alloys and different strategies have been proposed, for example alloying [27], mechanical deformation [28], hybridization of Mg alloy and biopolymers [29], and surface modification [30]. In particular, surface treatment is very attractive, because it is applicable to all types of alloys and only alters selective surface properties such as the bioactivity [31], antibacterial performance [32], and cell functions [33,34], while the favorable bulk attributes like mechanical properties are preserved.

The biocompatibility and surface biological functions are important considerations for biomaterials. Owing to the similar chemical composition with hydroxyapatite that is the inorganic

* Corresponding author at: Hubei Collaborative Innovation Center for Advanced Organic Chemical Materials, Ministry-of-Education Key Laboratory for the Green Preparation and Application of Functional Materials, Hubei Province Key Laboratory of Industrial Biotechnology, School of Materials Science & Engineering, Hubei University, Wuhan, China. Fax: +86 27 88665610.
E-mail addresses: shuilin.wu@gmail.com, sxwsl1976@163.com (S. Wu).

http://dx.doi.org/10.1016/j.corsci.2015.10.010
0010-938X/

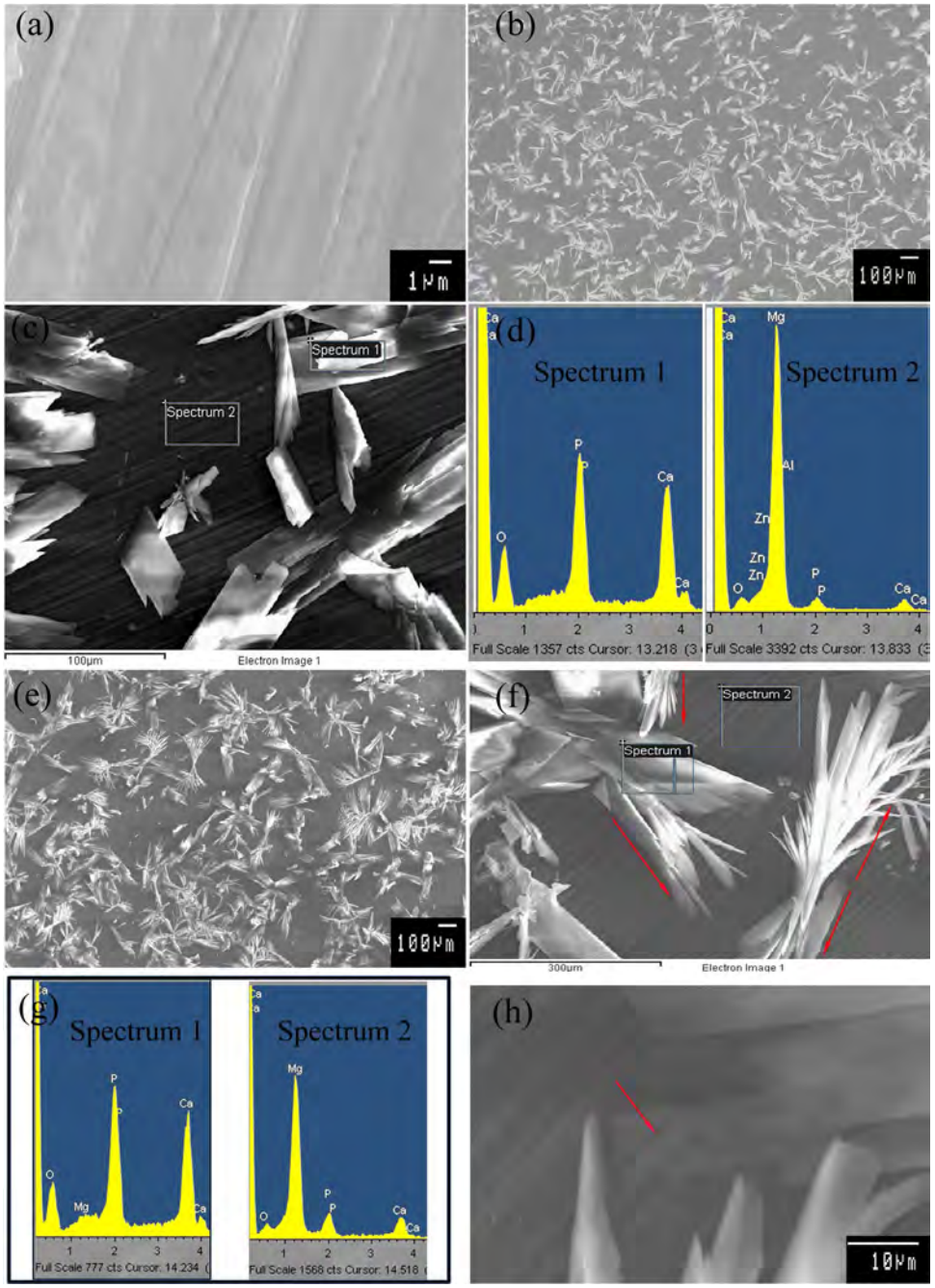

Fig. 1. Surface morphologies of magnesium alloys electrochemically deposited for different time at earlier stage, (a) substrate, (b) 5 min, (c) high magnification of image (b), (d) EDS spectra corresponding to image (c), (e) 10 min, (f) high magnification of image (e), (g) EDS spectra corresponding to image (f), (h) high magnification of image (e). (For interpretation of the references to color in this figure legend, the reader is referred to the web version of this article.)

component of natural bone, calcium phosphate (Ca–P) coatings are often deposited on biomaterials [35,36]. Common techniques to modify Mg alloys include plasma spraying [37], micro-arc oxidation [38], electrochemical deposition [39], sol–gel technique [40], chemical conversion coating [41], hydrothermal method [42], magnetron sputtering [43], and ion implantation [44]. Among these techniques, electrochemical deposition has received much attention because of the simplicity, low cost, and high efficiency. Furthermore, the structure and chemical composition of the coatings can be easily controlled by adjusting the electrochemical parameters. Ca–P coatings prepared by electrochemical deposition have been observed to suppress leaching of metallic ions from titanium alloys, enhance the osteoinductivity of metallic implants [45,46], and improve the corrosion resistance of Mg alloys [47,48], but defects, cracks, and poor adhesion can be drawbacks [49]. In order to improve the corrosion resistance to allow sufficient time for tissue healing, organic species can be incorporated into Ca–P coatings. Polymer coatings can also be utilized as drug carriers to deliver drugs and genes [50,51] while improving the corrosion resistance, wear, and abrasion properties of Mg alloys [52]. In particular, poly(lactic-co-glycolic acid) (PLGA) has good biocompatibility, and biodegradability and is non-toxic [53]. The corrosion rate of PLGA can be controlled by adjusting the ratio of the two co-monomers. Ostrowski et al. and Li et al. have reported that PLGA with different monomer ratios and concentrations enhances the corrosion resistance of Mg–Zn alloy and *in vitro* studies have revealed improved

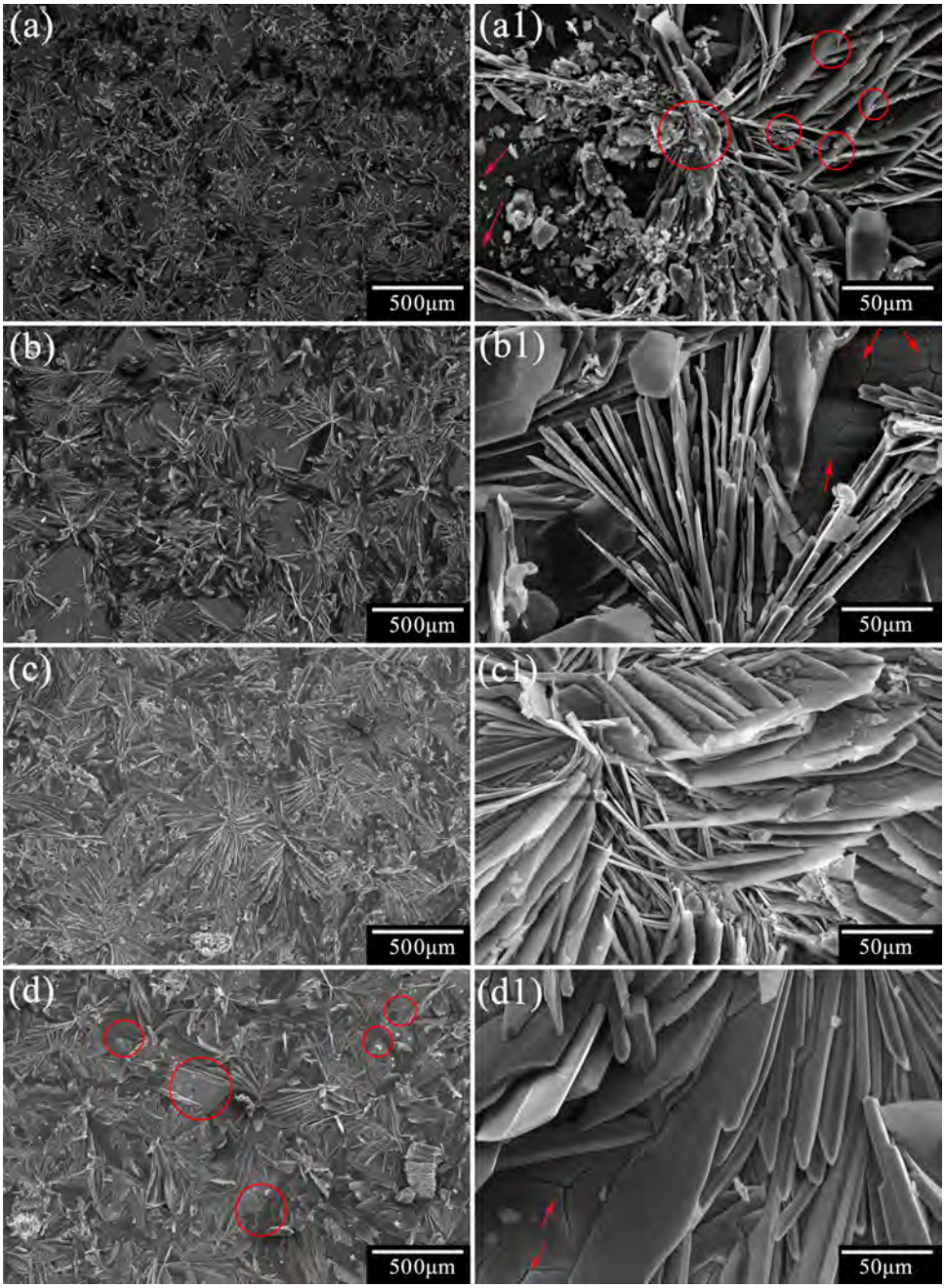

Fig. 2. Microstructure evolution of Ca–P coatings with different deposition time (a) 20 min, (a1) high magnification of image (a), (b) 60 min, (b1) high magnification of image (b), (c) 120 min, (c1) high magnification of image (c), (d) 240 min, (d1) high magnification of image (d). (For interpretation of the references to color in this figure legend, the reader is referred to the web version of this article.)

biocompatibility of PLGA coated AZ31 [54,55]. In this work, the structure and morphology of PLGA/Ca–P hybrid coatings as well as their effects on the corrosion resistance of AZ31 Mg alloys are systematically investigated.

2. Experiment details

2.1. Materials preparation

Commercial AZ31 Mg alloy (wt%: 3% Al, 1% Zn, 0.2% Mn, Fe < 0.005%, balanced Mg) with dimensions of $\varphi 16 \times 5$ mm were ground with SiC paper with different grit size (240, 600, 800, 1200, and 2400) successively, ultrasonically rinsed with acetone and ethanol for 15 min, and dried by flowing warm air.

2.2. Electrochemical deposition

The electrolyte used to form the Ca–P coatings contained 0.042 mol/L $Ca(NO_3)_2{\cdot}4H_2O$, 0.025 mol/L $NH_4H_2PO_4$ and 0.1 mol/L $NaNO_3$ and the pH was 4.5. The side of each sample was connected to copper wires and the whole sample except the polished surface was sealed with silica gel. Electrochemical deposition was carried out on the electrochemical analyzer (IT6500) at a constant cathodic voltage of 2.5 V with a graphite plate as the anode and the exposed surface of AZ31 as the cathode immersed in the electrolyte. By means of magnetic stirring (SZCL-4A), Ca–P deposition was performed at room temperature for different time durations between 5 and 240 min.

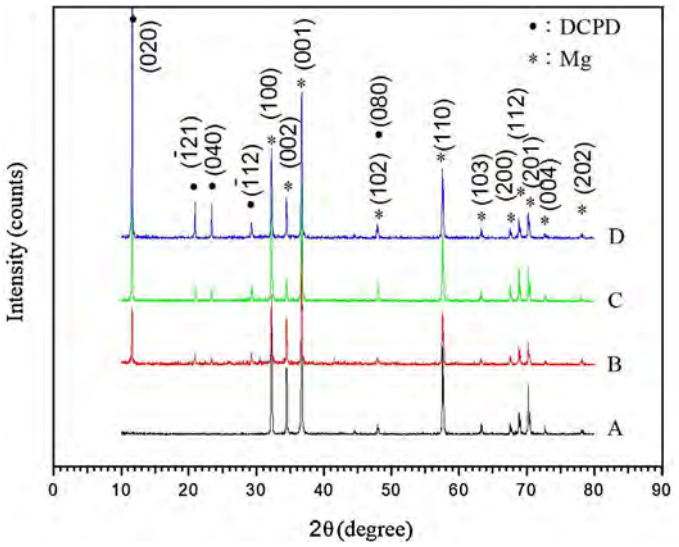

Fig. 3. XRD patterns of Mg alloys with different depostion time, (A) substrate, (B) 20 min, (C) 60 min, (D) 120 min.

2.3. Spin coating

The PLGA solution was prepared by dissolving the PLGA powder (average molecular weight M_W = 120,000, co-polymer ratio = 85:15) in chloroform and the PLGA concentration was 4% (w/v). Spin coating was conducted on the spin coater (KW-4A) at room temperature. One milliliter of PLGA was dropped onto the surface of the Ca–P coated sample at a rotating speed for 10 s to make sure that the solution reached the edge of the sample and afterwards, spinning was conducted at 5000 rpm for 30 s so that the solution spread to all the exposed area. The spin coating process was repeated three times followed by drying under N_2 and storage in an oven at room temperature.

2.4. Surface characterization

The morphology and composition of the coatings were determined on a scanning electron microscopy (SEM, JEOL-820 and JSM6510LV) equipped with energy-dispersive spectroscopy (EDS). The phase structure of the Ca–P coatings was analyzed by X-ray diffraction (XRD, D/MAX-IIIC, Rigaku) using a Cu Kα radiation (λ = 0.15406 nm) at 40 kV and 30 mA. The measurement was performed at diffraction angles between 10° and 80° in 2θ at a step size of 0.02°. The composition and structure of PLGA were determined by Fourier transform infrared spectroscopy (FT-IR, Nicolet570).

2.5. Electrochemical tests

The corrosion tests were carried out in simulated body fluid (SBF) at 37 °C on the CHI660E electrochemical analyzer using a 3-electrode cell configuration with the pre-treated specimen as the working electrode, platinum plate as the auxiliary electrode, and saturated calomel electrode as a reference electrode. The area exposed to SBF was 0.64 cm^2. The change in the open-circuit potential (OCP) was first monitored as a function of immersion time for about 4000 s. The potentiodynamic polarization tests were carried out at a scanning rate of 2 mV/s. The degradation rate was determined by the corrosion current (i_{corr}) obtained from the polarization curves by extrapolating the cathodic branch of the polarization curve to the corrosion potential (E_{corr}). After soaking in SBF for different time periods, the specimens were removed and dried at room temperature. The SBF with a pH of 7.4 was composed of 8 g/L NaCl, 0.35 g/L $NaHCO_3$, 0.25 g/L KCl, 0.2 g/L $K_2HPO_4{\cdot}3H_2O$, 0.3 g/L $MgCl_2{\cdot}6H_2O$, 0.28 g/L $CaCl_2$, 0.07 g/L Na_2SO_4, and 6 g/L $NH_2(CH_2OH)_3$ [56].

Electrochemical impedance spectroscopy (EIS) was conducted at the open circuit potential by applying a sinusoidal potential of 5 mV in the frequency range from 10^5 to 10^{-2} Hz. The software Zsimpwin 3.21 was used to simulate the impedance and study the corrosion mechanism. The EIS measurements were conducted three times to improve the statistics.

2.6. Hydrogen evolution

Both the coated and uncoated samples were immersed in Hank's solution at 37 °C to measure the hydrogen evolution rate. The ratio of the Hank's solution volume (mL) to the exposed area (cm^2) of the sample was 25:1. Hydrogen evolution was monitored for 240 h and the data were recorded at 2 h intervals in the first 12 h and then every 24 h.

3. Results and discussion

3.1. Microstructure evolution of Ca–P coatings

Fig. 1 shows the surface morphology of the Ca–P coated AZ31 magnesium alloys in the early stage. As shown in Fig. 1a, there are some scratches on the mechanically polished magnesium alloys. After deposition for 5 min in SBF, precipitates appear sparsely on the surface (Fig. 1b) and the high-magnification image discloses the flake-like structure (Fig. 1c). EDS shows that these precipitates consist of mainly Ca, P and O and no Mg signal is detected (spectrum 1 in Fig. 1d). The spectrum obtained from the scratched area without precipitates show intense Mg signal as well as those of Al and Zn from the substrate. Weak Ca and P peaks can also be detected (spectrum 2 in Fig. 1d) indicating nucleation and growth of Ca–P on the surface. In comparison with Fig. 1b, the size of the precipitates after deposition for 10 min increases (Fig. 1e). The high-magnification image reveals that the flake-like precipitates grow preferentially along the axis in the initial stage as shown by the red arrows in Fig. 1f. EDS shows the presence of Ca, P and O in the plate-like precipitates (spectrum 1 in Fig. 1g) and a trace of Mg from the substrate. Some initially nucleated Ca–P plates are very thin and almost transparent as marked the red arrow in Fig. 1h. The EDS spectrum (spectrum 2 in Fig. 1g) obtained from the area without precipitates shows stronger signals of Ca and P than those in Fig. 1d. Compared to Fig. 1d, the intensity of Mg decreases and Al and Zn are not detected. It suggests that 10 min deposition induces the formation of a thicker Ca–P film on the exposed area compared to 5 min.

As the deposition time is increased, the plate-like Ca–P phase continues to grow as shown in Fig. 2. In comparison with the samples deposited for 20 min and 60 min shown in Fig. 2a and b, respectively, when the deposition time reaches 120 min, the surface is fully covered by the compact Ca–P coating (Fig. 2c and c1). However, when the time is further increased to 240 min, some areas are not covered by the flake-like Ca–P phases (indicated by red arrows in Fig. 2d1) possibly due to the decrease in the Ca and P concentrations in the solution in this stage. There appears to be a dynamic balance between electrochemical deposition and Ca–P coating dissolution and our results reveal an optimal deposition of 120 min and further deposition actually accelerates dissolution of the coatings. Besides the size and distribution, the evolution of the coating is quite different from that in the early stage (Fig. 1). The Ca–P phases grow from the center toward two sides in the early stage (Fig. 1f) while there are many small branches with new centers diverging from the center toward the periphery as the deposition time is increased (marked by red circles in Fig. 2a1).

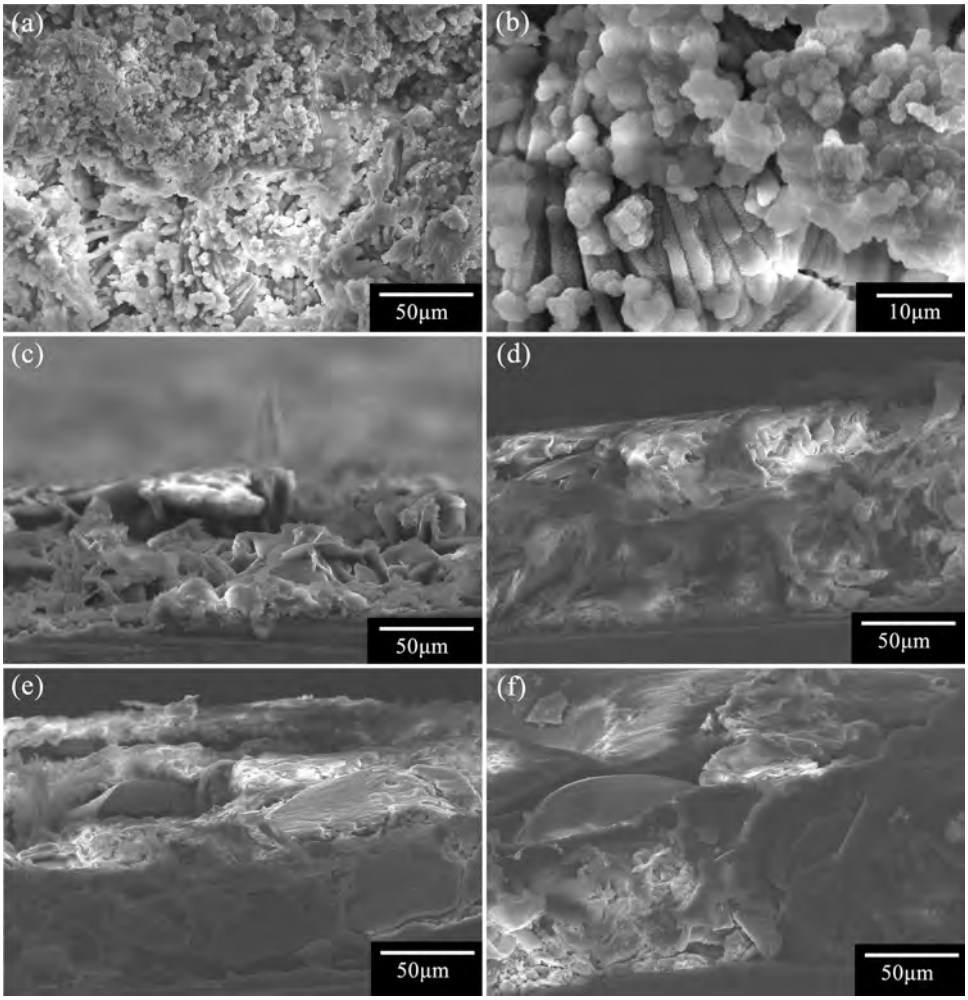

Fig. 4. SEM images of hybrid coatings before corrosion. (a) 20 min DCPD deposition; (b) high magnification image of (a); cross section of hybrid coating with different DCPD deposition, (c) 20 min, (d) 60 min, (e) 120 min, (f) 240 min.

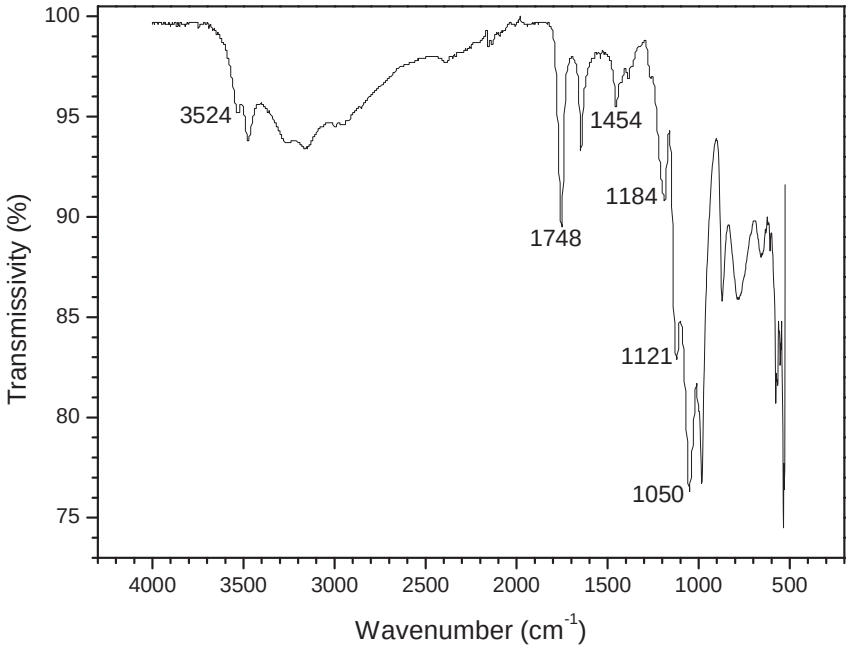

Fig. 5. FTIR spectra of DCPD/PLGA hybrid coatings.

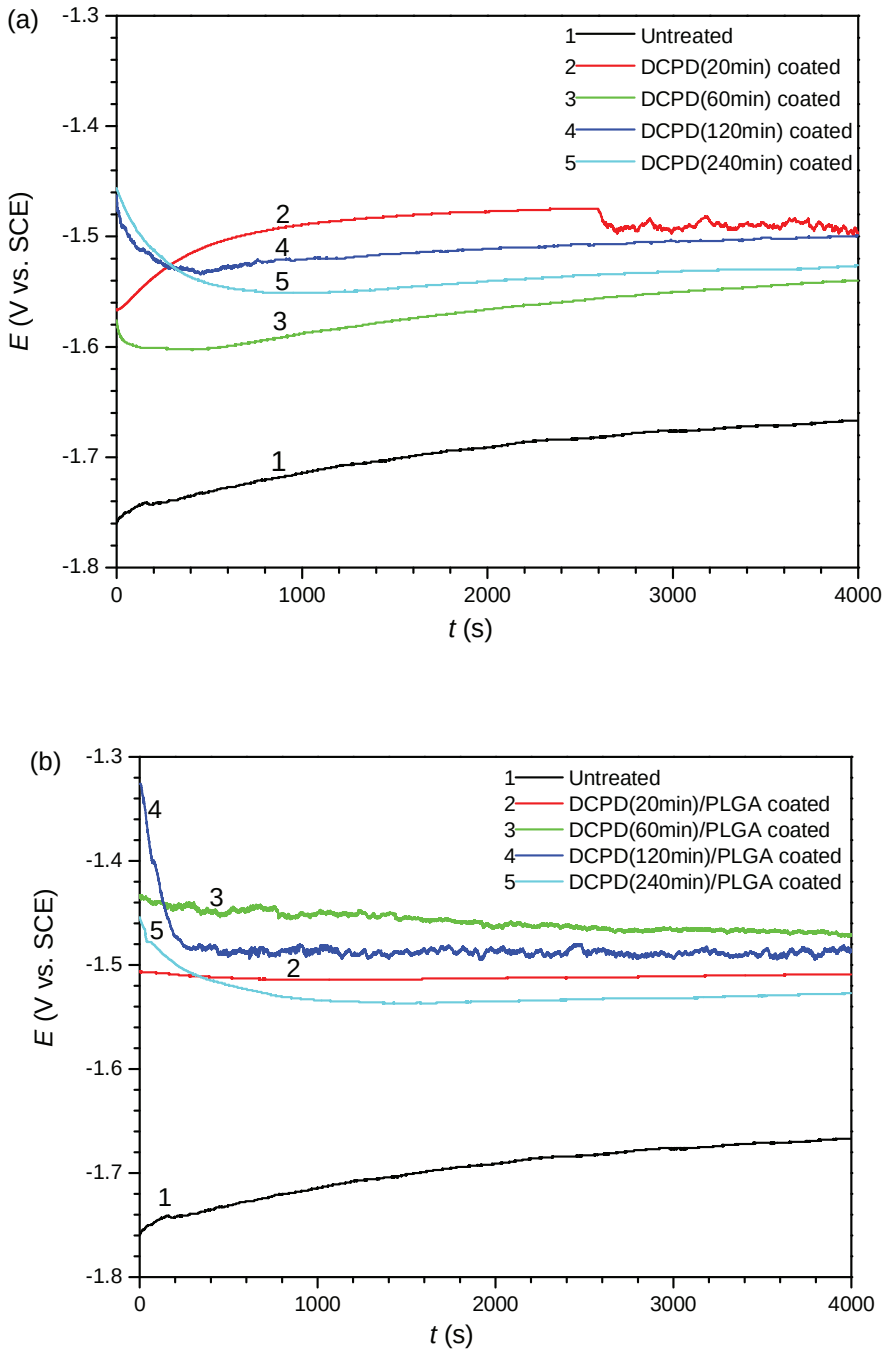

Fig. 6. Open circuit potentials evolution for (a) DCPD coatings, and (b) DCPD/PLGA hybrid coatings.

Furthermore, small cracks occur on the surface after deposition for 20 min (indicated by red arrows in Fig. 2a1) and become larger as the deposition time is increased (marked by red arrows in Fig. 2b1 and d1). It may be due to the local reaction between metallic Mg and water in the solution leading to release of hydrogen and crack formation.

The phase composition of the electrochemically deposited coatings is characterized by XRD. As shown in Fig. 3, the substrate shows the typical XRD pattern of Mg–Zn alloys [11,57,58]. The Ca–P coatings are composed of predominantly $CaHPO_4{\cdot}2H_2O$ crystal and dicalcium phosphate dihydrate (DCPD) but no other Ca–P phases are detected. Mg peaks are observed clearly from the DCPD coated alloys indicating that DCPD coatings are quite thin. As shown in Fig. 3, the intensity of the Mg peaks, *i.e.*, Mg (0 0 1), (1 0 0), and (1 1 0), decreases gradually with deposition time because the newly formed DCPD coatings cover the surface and become thicker. The increasing intensity of DCPD peaks (0 2 0), ($\bar{1}$21), (0 4 0) and ($\bar{1}$12)provides addition evidence and is in accordance with the EDS results in Fig. 1d and g.

3.2. Characterization of DCPD/PLGA hybrid coating

As shown in Fig. 4a, after spinning, the DCPD coating almost cover the PLGA layer fully. Some of the cracks, pores, and space between the DCPD plates and even the DCPD plates are filled with PLGA (Fig. 4b). Fig. 4c–f show the cross-sectional images of the hybrid coating deposited for different time.As the time is increased, the coatings become thicker. Similar to the morphology in Fig. 4a,

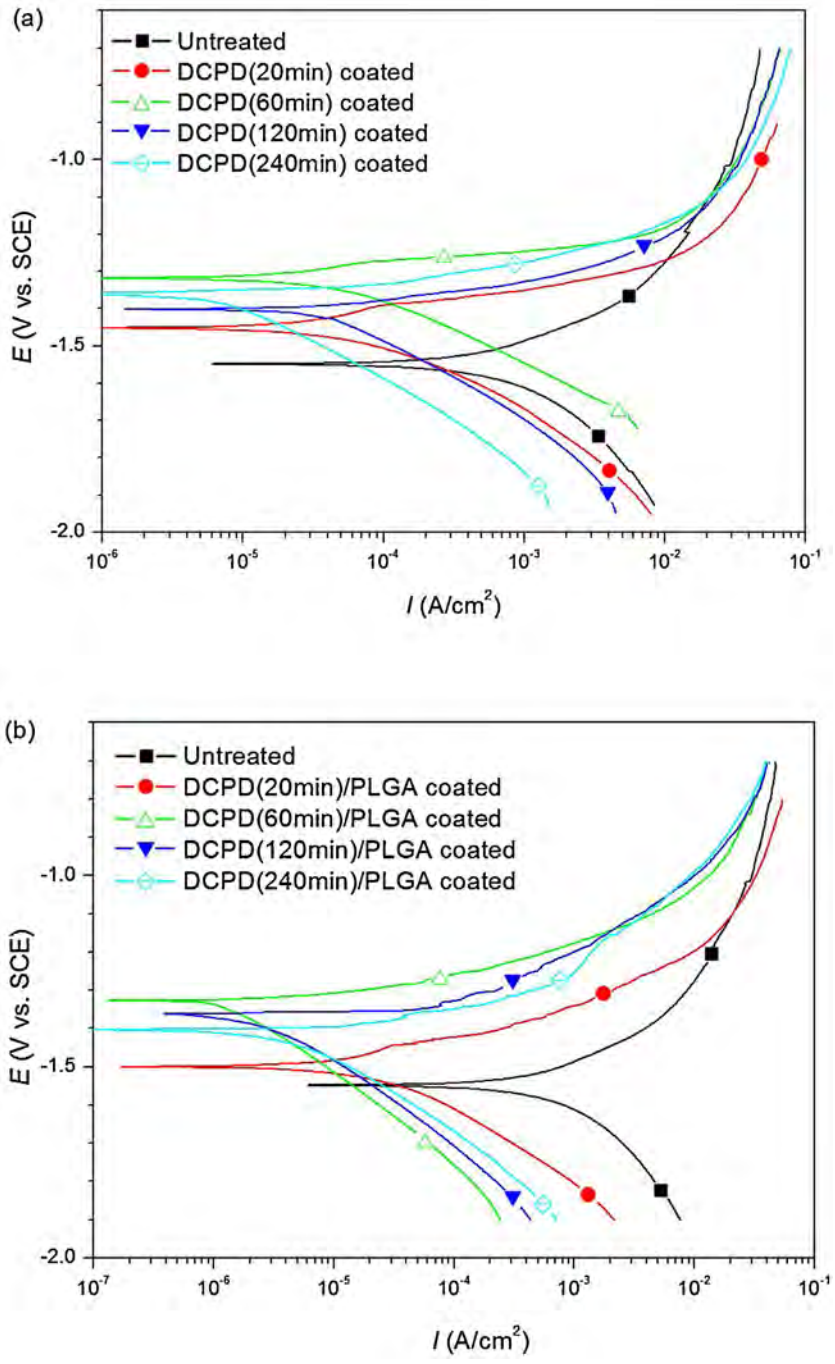

Fig. 7. Potentiodynamic polarization tests of Mg alloys in SBF coated with (a) DCPD, and (b) DCPD/PLGA.

PLGA not only covers the surface of the DCPD plates, but also penetrates into the bottom and even the surface of the Mg alloy. The FTIR result acquired from the DCPD/PLGA coating is depicted in Fig. 5. The characteristic absorption peak of PLGA at 1748 cm^{-1} is related to C=O stretching of the ($-COO^-$) group and those at 1184, 1121, and 1050 cm^{-1} are attributed to the C—O group. The peak at 1454 cm^{-1} is attributed to $-CH_2-$ stretching and that at 3520 cm^{-1} corresponds to O—H stretching. The results demonstrate that PLGA is fabricated on the DCPD coated samples by spin coating.

3.3. Electrochemical measurements

The open circuit potentials (OCPs) of AZ31 with the DCPD and hybrid coatings are determined in SBF at 37 °C. As shown in Fig. 6a, the initial OCP values fluctuates in the early stage (0–1000 s) for all the DCPD coated samples while this only lasts for 600 s for the DCPD/PLGA coated AZ31 (Fig. 6b), implying that the latter becomes stable sooner. Generally, the DCPD coating enhances the OCP of the alloy. The drop in the OCP implies film breakdown (curve 2 in Fig. 6a) whereas the slight increase (curves 3–5) in the OCP indicates formation of a new layer, i.e, corrosion products, deposit, or precipitate in SBF. Fig. 6b shows small fluctuations (shown in curves 2–5) even in this stable state possibly caused by swelling and rupturing of the PLGA film and formation of corrosion products because water can penetrate the PLGA film to the substrate. With regard to the untreated Mg alloy, curve 1 in Fig. 6 increases gradually up to 3000 s and then is nearly constant afterwards, suggesting that the untreated Mg alloys corrodes rapidly initially and then are covered

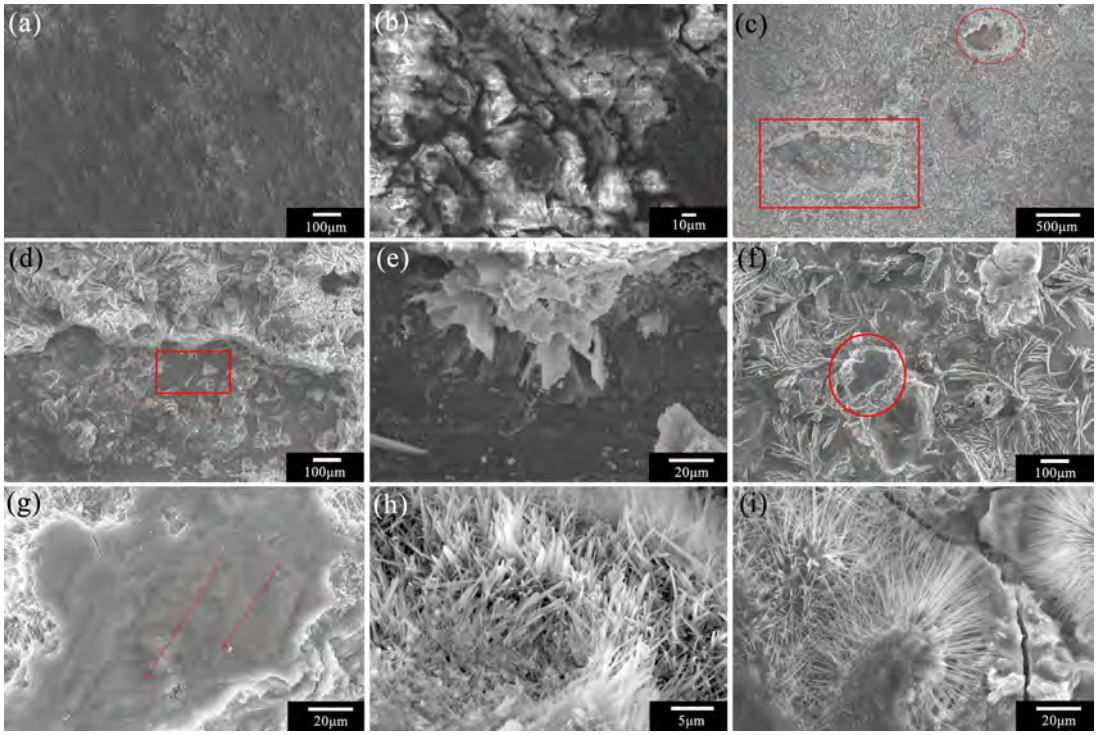

Fig. 8. Surface morphologies of corroded Mg alloys with different deposition time: (a) substrate, (b) high magnification image of (a), (c) 120 min, (d) high magnification image of area marked by red rectangle in (c), (e) high magnification image of area marked by red rectangle in (d), (f) 240 min, (g) high magnification image of area marked by red circle in (f), (h) high magnification image of (g), (i) high magnification image of (f). (For interpretation of the references to color in this figure legend, the reader is referred to the web version of this article.)

by the corrosion products. In general, the DCPD/PLGA hybrid coatings show higher and more stable OCP values than the DCPD coated ones as well as untreated Mg alloys.

In comparison with weight loss test, electrochemical potentiodynamic polarization tests can accelerate the corrosion process and can evaluate the corrosion resistance or degradation rate in a relatively short time. Fig. 7a shows the potentiodynamic polarization curves of the Mg alloys in SBF. The measured i_{corr} of the untreated Mg alloy is 5.4×10^{-4} A/cm^2, whereas the i_{corr} values of all the DCPD coated Mg samples are reduced by almost an order of magnittue, indicating that the DCPD coatings significantly enhance the corrosion resistance of the Mg alloy. In particular, 240 min deposition results in the smallest i_{corr} of 1.19×10^{-5} A/cm^2. The degradation behavior depends on the surface structure. The uncoated Mg alloy is exposed directly to SBF and Mg reacts with H_2O resulting in rapid degradation of Mg. In principle, samples deposited for a longer time should exhibit much better corrosion resistance because more DCPD crystals precipitate but in reality, cracks become larger (marked by red arrow in Fig. 2b1) undermining the protection rendered by the DCPD.Therefore, the i_{corr} values are similar. The slight enhancement in the E_{corr} is due to the thicker coating after a longer deposition time. There is a slight difference between the E_{corr} and i_{corr} of the DCPD-coated samples. The 60 min sample has an E_{corr} of −1.37 V whereas the 120 min sample shows an i_{corr} of 7.86×10^{-5} A/cm^2 due to the limitation of the polarization technique to evaluate the *in vitro* corrosion rate of Mg alloys because the anodic polarization curves of Mg and its alloys do not obey the Tafel Law [59,60].

Fig. 7b presents the potentiodynamic polarization curves of the different DCPD/PLGA coated samples in SBF. In comparison with the uncoated and DCPD-coated magnesium alloys, the hybrid coatings (except 240 min coating) show lower i_{corr} indicating that PLGA enhances the corrosion resistance of the DCPD-coated samples to some extent. Meanwhile, the corrosion resistance of the DCPD/PLGA hybrid coatings can be regulated by the deposition time. The PLGA minimizes the defects in the DCPD coatings to enhance the corrosion resistance and it is in good agreement with the observation shown in Fig. 4. Similar results have been obtained by Gnedenkov et al. [53].

Fig. 8 shows the surface morphology of the corroded Mg alloys after electrodynamic polarization tests in SBF at 37 °C. The uncoated Mg alloys are subjected to severe corrosion and cracks and island-like structure emerge from almost the entire surface (Fig. 8a and b). The crack has an average size of about 10 μm.This phenomenon is caused by the chemical reaction between Mg and the solution as shown in the following [1,15]:

$$Mg + 2H_2O \rightarrow Mg(OH)_2 + H_2 \uparrow \quad (1)$$

Potentiodynamic polarization accelerates release of hydrogen and formation of cracks and so the untreated Mg alloys has the highest degradation rate. In contrast, the DCPD coating (120 min) is relatively intact in spite of scattered corroded pits (marked by red circles in Fig. 8c). As shown in Fig. 8d, the compact DCPD retains the original flake-like structure and the 120 min DCPD coating is quite thick even after the electrochemical corrosion tests. No corrosion can be observed from the debonded area except cracks in the residual coating (Fig. 8d). The high-magnification image in Fig. 8e shows the remaining plate-like phases on the intact substrate that is quite different from the corroded substrate as shown in Fig. 8a and b. It is consistent with the potentiodynamic polarization tests. The corroded surface of the 240 min sample is displayed in Fig. 8f. Unlike the 120 min sample, cracks can be observed from the entire surface (Fig. 8f and i) and a part of the substrate is exposed and degraded during the corrosion tests due to the exfoliation of coatings as confirmed by the mechanical scratches indicated by red arrows in Fig. 8g. However, new materials are formed on the corroded area. The high-magnification images reveal that these newly formed materials are one dimensional nanowires (Fig. 8h and i)

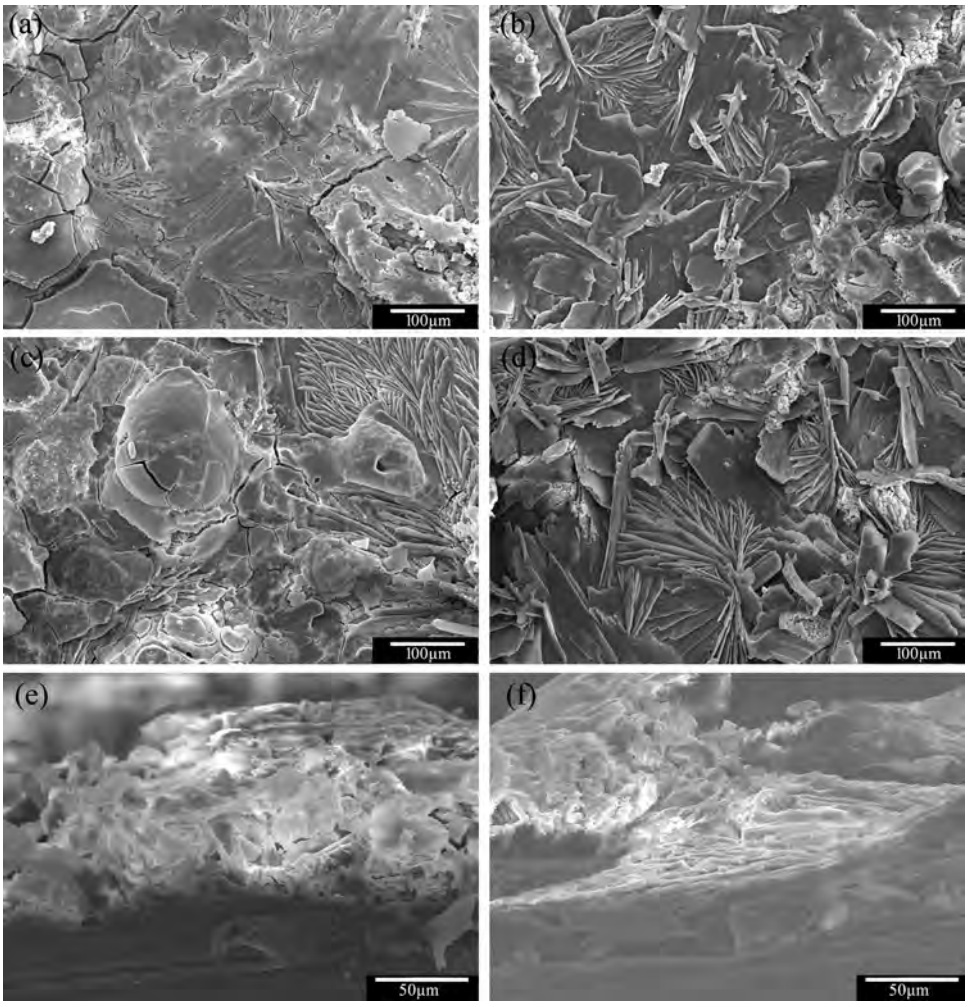

Fig. 9. Surface and cross section images of corroded DCPD/PLGA coatings with different DCPD deposition time: (a) 20 min, (b) 60 min, (c) 120 min, (d) 240 min, cross section of (e) 20 min, (f) 240 min.

possibly playing a self-repairing function during the corrosion process.

Fig. 9 shows the surface morphology and cross section of the corroded Mg alloys with DCPD/PLGA hybrid coatings after electrodynamic polarization tests in SBF at 37 °C. Regardless of the DCPD depotision time, unlike the pure DCPD coating (Fig. 8), all the hybrid coatings retain the original surface morphology without the appearance of corrosion pits after the corrosion tests. For instance, the 240 min hybrid coating shows fewer corroded areas and cracks than the DCPD-coating in Fig. 8f, indicating that PLGA enhances the corrosion resistance significantly.

EIS is employed to assess the corrosion performance of the uncoated, DCPD, and DCPD/PLGA coated samples in SBF as shown in Fig. 10. The EIS behavior of the coated samples is distinctly different from that of the untreated specimen. For both the DCPD and DCPD/PLGA coated samples, larger capacitive loops are shown in Fig. 10a and b, indicating that the corrosion resistance of the coated Mg alloy is much higher than that of the untreated sample. In addition, compared to the capacitive loop of the DCPD coated sample (Fig. 10a), the diameter of the capacitive loop of the DCPD/PLGA coated specimen increases significantly (Fig. 10b), indicating that both the DCPD and DCPD/PLGA hybrid coatings can protect the Mg alloy from corrosion and the latter can enhance the corrosion resistance more effectively. Shi et al. have studied the corrosion resistance of poly-lactic acid (PLA)/micro-arc oxidation (MAO) composite coatings by electrochemical tests and immersion tests in SBF and found that the composite coating is a good choice to prevent the Mg alloy from degradation in comparison with the PLA or MgO coating [59]. The EIS bode plots of the bare and coated AZ31 alloy during immersion in SBF are shown in Fig. 11. The values of the modulus of impedance measured at 0.01 Hz from the DCPD coating are larger than those of the bare alloy (shown in Fig. 11a) and the hybrid coating has the largest values (Fig. 11c). Because of the relaxation reaction of the intermediate products between the substrate and DCPD coating, an obvious inductive loop appears from all the curves in the low frequency region between 1 and 0.01 Hz (Fig. 11a and c) and it is consistent with results obtained from inorganic coatings with a similar structure [30].

Table 1
Fitting results of EIS plots using EC1.

$R_S(\Omega\,cm^2)$	$C_1(\Omega^{-1}\,cm^{-2}\,s^{-n})$	$R_1(\Omega\,cm^2)$	$R_2(\Omega\,cm^2)$	$C_2(\Omega^{-1}\,cm^{-2}\,s^{-n})$
4.57	1.02×10^{-5}	210	46.6	1.4×10^{-4}

The corresponding equivalent circuit (EC) models for the EIS spectra are presented in Fig. 12. The EC1 model shown in Fig. 12a is widely accepted for modeling of a surface film with oxide layers due to natural oxidation of Mg during mechanical polishing [61]. Here, Rs is the SBF resistance, R_1 and C_1 refer to the resistance and capacitance of the out loose layer, respectively, and R_2 and C_2 are the resistance and capacitance of the inner barrier layer, respectively.

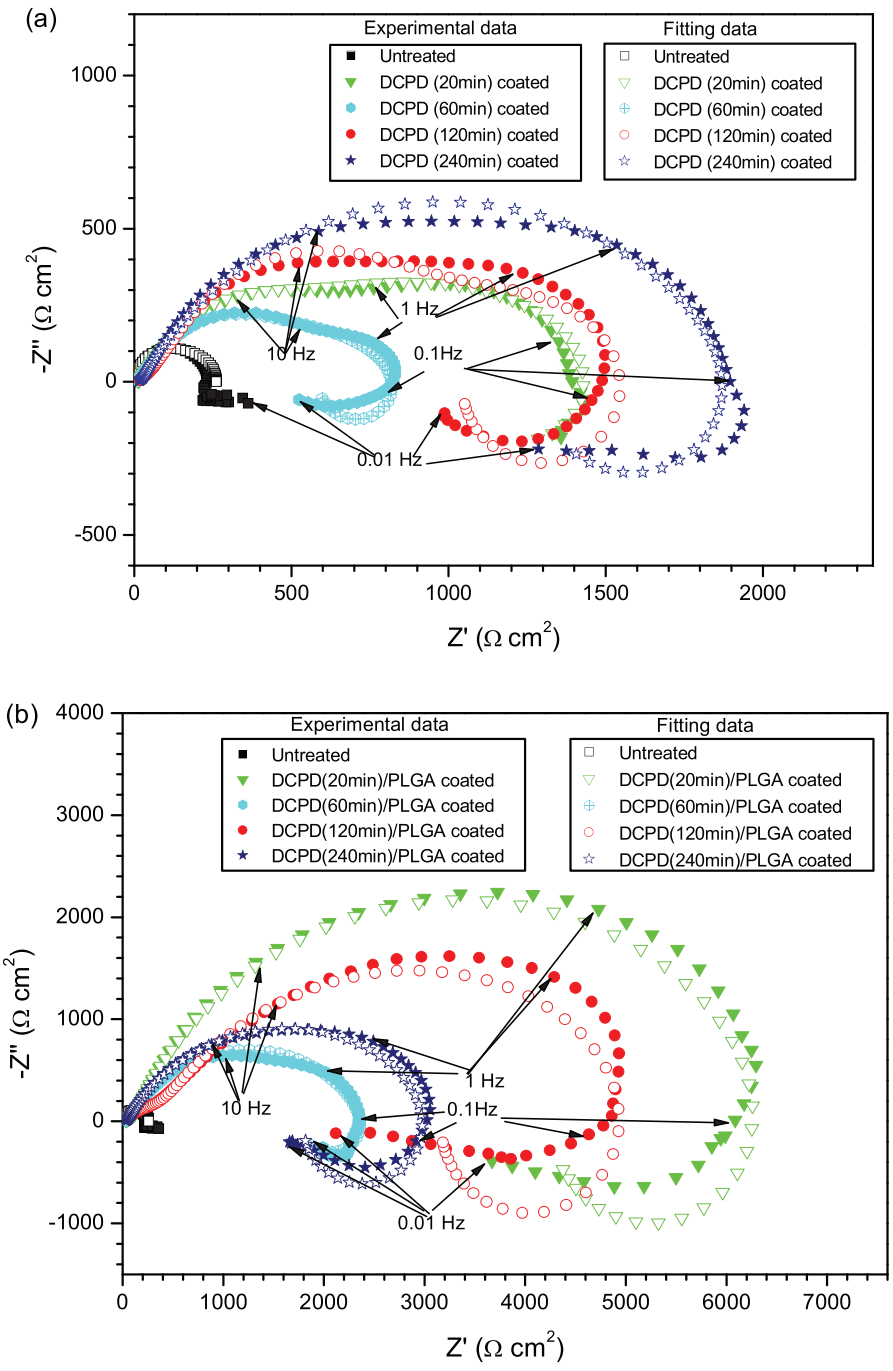

Fig. 10. Nyquist plots of AZ31 coated with (a) DCPD, and (b) DCPD/PLGA.

Table 2
Fitting results of EIS plots using EC2.

Time	R_S (Ω cm^2)	C_1 (Ω^{-1} cm^{-2} s^{-n})	R_1 (Ω cm^2)	R_2 (Ω cm^2)	Q_1 (Ω^{-1} cm^{-2} s^{-n})	n	R_L (Ω cm^2)	L (H cm^2)
20 min	9.35	1.99×10^{-5}	234	1.42×10^{3}	1.99×10^{-4}	0.533	1.99×10^{3}	1.2×10^{5}
60 min	9.06	1.93×10^{-5}	1.88×10^{3}	683	1.74×10^{-4}	0.8	911	5.55×10^{3}
120 min	12.8	2.25×10^{-5}	503	1.55×10^{3}	3.55×10^{-2}	0.448	834	3.79×10^{3}
240 min	14.2	7.80×10^{-7}	74.1	1.93×10^{3}	5.26×10^{-5}	0.696	3.72×10^{3}	4.16×10^{4}

Table 3
Fitting results of EIS plots using EC3.

Time	R_S (Ω cm^2)	R_1 (Ω cm^2)	Q_0 (Ω^{-1} cm^{-2} s^{-n})	n	R_2 (Ω cm^2)	Q_1 (Ω^{-1} cm^{-2} s^{-n})	n	L (H cm^2)	R_L (Ω cm^2)
20 min	23.1	14.5	1.14×10^{-5}	0.658	6.62×10^{3}	1.29×10^{-5}	0.786	6.16×10^{4}	1.08×10^{4}
60 min	21.1	5.8	1.25×10^{-5}	0.647	2.37×10^{3}	2.09×10^{-5}	0.684	5.07×10^{4}	5.88×10^{3}
120 min	23.5	604	1.64×10^{-5}	0.539	5.1×10^{3}	1.73×10^{-5}	0.708	1.63×10^{4}	5.13×10^{3}
240 min	22.1	84.3	3.05×10^{-5}	0.596	3.19×10^{3}	8.47×10^{-6}	0.763	1.54×10^{4}	3.59×10^{3}

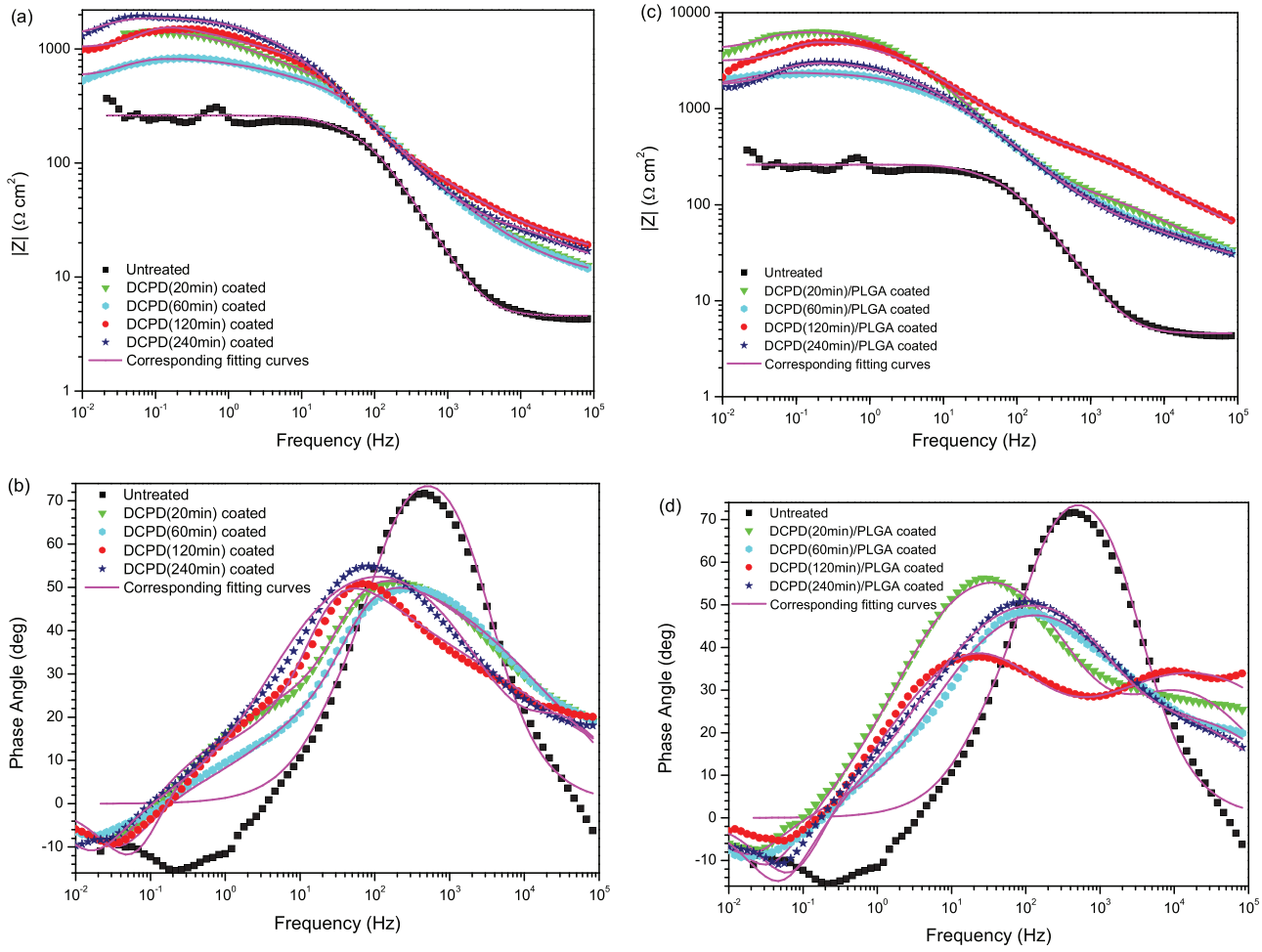

Fig. 11. EIS Bode plots obtained for the untreated and coated AZ31 alloy during immersion in SBF: (a and b) DCPD coating, and (c and d) DCPD/PLGA coating.

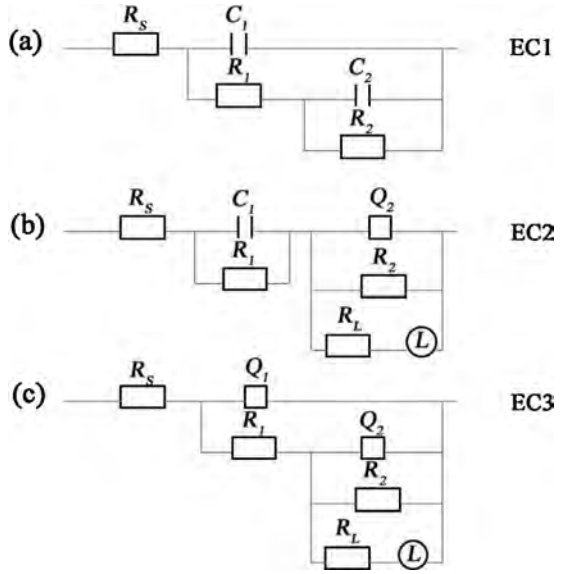

Fig. 12. Equivalent circuits used to fit the EIS diagrams for (a) the untreated Mg alloy, R(CR(CR)); (b) DCPD coated, R(CR)(QR(RL)); and (c) DCPD/PLGA coated, R(Q(R(QR(RL)))).

The different shape of the EIS spectra of the DCPD and DCPD/PLGA coated samples (shown in Fig. 10) suggests different structures. Accordingly, the EIS spectra are fitted with the corresponding models of EC2 and EC3 (Fig. 12b and c), respectively. The fitted results are listed in Tables 1–3. As shown in Table 1, the smaller R_2 indicates the thin and loose structure of the native oxide layer on the uncoated samples. In EC2 and EC3, R_L and L represent the resistance and inductance of the species absorbed onto the coatings [61,62] and Q, a constant phase element (CPE), is used instead of a capacitive element and the admittance, Y, of the CPE element and can be caculated by the formula (Y_{CPE} $(\omega) = 1/Z_{CPE} = Q_a(j\omega)^n$) [63]. In view of the more complicated outer structure of DCPD/PLGA hybrid coatings, Q_1, a *CPE* in EC3, is used to substitute for the capitance of C_1 in EC1 and EC2. During immersion in SBF, the entire surface of the uncoated Mg alloys is corroded accompanied by the formation of corrosion products such as magnesium hydroxide, carbonate, and phosphate [62]. However, the DCPD coating prevents the penetration of SBF into the sample leading to a larger R_2 (Table 2) compared to the bare sample, suggesting the formation of a compact inner layer of DCPD on the Mg alloy. The fluctuation in R_1 in Table 2 indicates that the outer structure of the DCPD coating varies with deposition time (similar to Figs. 1 and 2). The fitted results of the DCPD/PLGA coated Mg alloy are shown in Table 3.The hybrid coatings have smaller Q_2 and larger higher R_2 than the DCPD coatings.The smaller Q_2 can be attributed to the thicker inner layer according to the equation of $d = \epsilon A/C$, where ϵ is the permittivity of

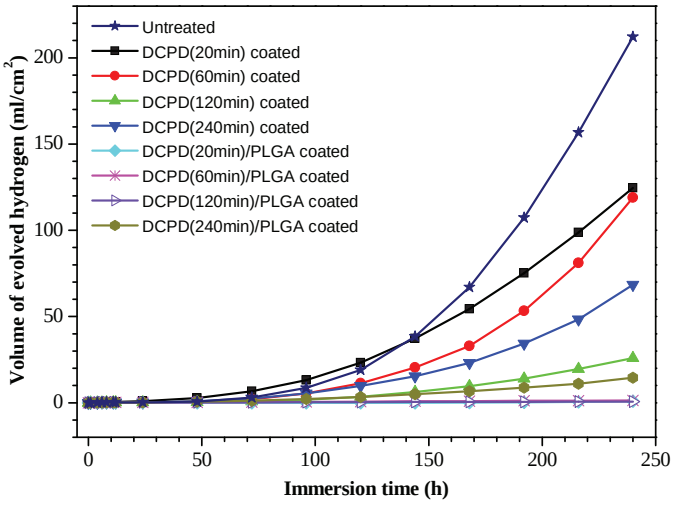

Fig. 13. Hydrogen evolution rates of the untreated, DCPD and DCPD/PLGA coated AZ31 in Hank's solutions.

the coating and A and d are the area and separation of the coatings, respectively [64]. A larger R_2 means that the inner layer of the coating becomes more compact after PLGA spin coating. Under the same conditions, the hybrid coating has larger R_2 and smaller Q_2, indicating that the PLGA on the DCPD coated sample further improves the corrosion resistance. In addition, R_2 in Table 3 also varies with deposition time of DCPD, suggesting that the structure of DCPD/PLGA hybrid coating is influenced by the surface morphology, structure, and thickness of DCPD coating. It is suggested that the carboxyl groups in the PLGA may react with the hydroxyl groups produced on the surface of Mg alloy to form Mg—O chemical bonds [60] and the protective effect of the composite coatings is quite different from that of a single film. For instance, the 20 min DCPD coated Mg alloy has a sparse film leading to better coverage of PLGA on the surface. The 240 min DCPD coating has a branched structure with a large size resulting in a more complex structure with more pores and gaps.Thus, some PLGA particles are not be able to penetrate the pores. This is the reason why the 20 min hybrid coating shows a larger R_2 than the 240 min hybrid coating. EIS demonstrates that the DCPD/PLGA hybrid coating improves the corrosion resistance similar to the polarization results. Based on the data, the degradation mechanism is postulated as follows. Degradation of PLGA produces acidic products which can react with $Mg(OH)_2$ to form Mg glycolates or Mg lactates [54,65] which can protect the film from corrosion. The DCPD inner coating acting as a barrier between the substrate and solution plays an important role in the corrosion protection. If the coating is too thin, the substrate is easily exposed to the solution and a large amount of OH^- is released to react with H^+ inducing fast corrosion [66].

3.4. Immersion testing

The hydrogen evolution rates (HERs) of the AZ31 samples are shown in Fig. 13. Compared to the bare sample, the DCPD and PLGA/DCPD coated Mg samples show lower HERs. The PLGA coating reduces the HERs and it is in agreement with the aforementioned results. In comparison to the electrochemical tests, there is a slight difference in the degradation rates of the hybrid coating with deposition time possibly due to PLGA degradation. Electrochemical tests are conducted for a short time but the hydrogen evolution tests are performed for a longer time. For the former, the effects of PLGA degradation is negligible but for the latter, PLGA degradation may produces acidic products that can react with $Mg(OH)_2$ to form Mg glycolates or Mg lactates [54,65] consequently affecting the corrosion behavior of the DCPD/PLGA coated Mg alloy.

4. Conclusion

DCPD and hybrid DCPD/PLGA are prepared on AZ31 Mg alloy by electrochemical deposition and spin coating. By changing the deposition time, the structure and morphology of the coatings in conjunction with the corrosion resistance can be controlled. EIS and potentiodynamic polarization tests show that both the DCPD and DCPD/PLGA coatings reduce the corrosion rate of the Mg alloy in SBF a longer deposition time generally leads to better corrosion protection. PLGA coverage can further enhance the corrosion resistance of DCPD by filling the cracks and pores. The hybrid coating not only regulates the degradation rate, but also is favorable to cell and tissue growth as a result of the good biocompatibility of DCPD.

Acknowledgements

This study was jointly supported by the Special Prophase Program for Key Basic Research of the Ministry of Science and Technology of China (973 Program), grant no. 2014CB660809; the National Natural Science Foundation of China, grant nos. 51422102, and 81271715; the Hong Kong Research Grants Council (RGC) General Research Funds (GRF) No. 112212, City University of Hong Kong Strategic Research Grant (SRG) No. 7004188, and Hubei Provincial Natural Science Foundation, grant nos. 2013CFA018 and 2014CFB551.

References

[1] Y.F. Zheng, X.N. Gu, F. Witte, Biodegradable metals, Mater. Sci. Eng. R 77 (2014) 1–34.
[2] M.P. Staiger, A.M. Pietak, J. Huadmai, G. Dias, Magnesium and its alloys as orthopedic biomaterials: a review, Biomaterials 27 (2006) 1728–1734.
[3] S.L. Wu, X.M. Liu, K.W.K. Yeung, C.S. Liu, X.J. Yang, Biomimetic porous scaffolds for bone tissue engineering, Mater. Sci. Eng. R 80 (2014) 1–36.
[4] N. Li, Y.F. Zheng, Novel magnesium alloys developed for biomedical application: a review, J. Mater. Sci. Technol. 29 (2013) 489–502.
[5] G.S. Wu, W. Dai, L.X. Song, A.Y. Wang, Surface microstructurization of a sputtered magnesium thinfilm via a solution-immersion route, Mater. Lett. 64 (2010) 475–478.
[6] M. Niinomi, M. Nakai, J. Hieda, Development of new metallic alloys for biomedical applications, Acta Biomater. 8 (2012) 3888–3903.
[7] N.T. Kirkland, N. Birbilis, M.P. Staiger, Assessing the corrosion of biodegradable magnesium implants: a critical review of current methodologies and their limitations, Acta Biomater. 8 (2012) 925–936.
[8] S. Shadanbaz, G.J. Dias, Calcium phosphate coatings on magnesium alloys for biomedical applications: a review, Acta Biomater. 8 (2012) 20–30.
[9] P.C. Banerjee, R.K.S. Raman, Y. Durandet, G. McAdam, Electrochemical investigation of the influence of laser surface melting on the microstructure and corrosion behaviour of ZE41 magnesium alloy—an EIS based study, Corros. Sci. 53 (2011) 1505–1514.
[10] C. Janning, E. Willbold, C. Vogt, J. Nellesen, A. Meyer-Lindenberg, H. Windhagen, F. Thorey, F. Witte, Magnesium hydroxide temporarily enhancing osteoblast activity and decreasing the osteoclast number in peri-implant bone remodeling, Acta Biomater. 6 (2010) 1861–1868.
[11] X.N. Gu, Y.F. Zheng, Y. Cheng, S.P. Zhong, T.F. Xi, *In vitro* corrosion and biocompatibility of binary magnesium alloys, Biomaterials 30 (2009) 484–498.
[12] J.M. Seitz, R. Eifler, F.W. Bach, H.J. Maier, Magnesium degradation products: effects on tissue and human metabolism, J. Biomed. Mater. Res. A 102 (2014) 3744–3753.
[13] T. Kraus, S.F. Fischerauer, A.C. Hanzi, P.J. Uggowitzer, J.F. Loffler, A.M. Weinberg, Magnesium alloys for temporary implants in osteosynthesis: *in vivo* studies of their degradation and interaction with bone, Acta Biomater. 8 (2012) 1230–1238.
[14] Z.J. Li, X.N. Gu, S.Q. Lou, Y.F. Zheng, The development of binary Mg–Ca alloys for use as biodegradable materials within bone, Biomaterials 29 (2008) 1329–1344.
[15] R.C. Zeng, Y. Hu, S.K. Guan, H.Z. Cui, E.H. Han, Corrosion of magnesium alloy AZ31: the influence of bicarbonate sulphate, hydrogen phosphate and dihydrogen phosphate ions in saline solution, Corros. Sci. 86 (2014) 171–182.
[16] X.N. Gu, X.H. Xie, N. Li, Y.F. Zheng, L. Qin, *In vitro* and *in vivo* studies on a Mg–Sr binary alloy system developed as a new kind of biodegradable metal, Acta Biomater. 8 (2012) 2360–2374.

[17] E.L. Zhang, L. Yang, J.W. Xu, H.Y. Chen, Microstructure, mechanical properties and bio-corrosion properties of Mg–Si(-Ca Zn) alloy for biomedical application, Acta Biomater. 6 (2010) 1756–1762.
[18] M.H. Tsaia, M.S. Chen, L.H. Lin, M.H. Lin, C.Z. Wu, K.L. Ou, C.H. Yu, Effect of heat treatment on the microstructures and damping properties of biomedical Mg–Zr alloy, J. Alloys Compd. 509 (2011) 813–819.
[19] M. Badar, H. Lunsdorf, F. Evertz, M.I. Rahim, B. Glasmacher, H. Hauser, P.P. Mueller, The formation of an organic coat and the release of corrosion microparticles from metallic magnesium implants, Acta Biomater. 9 (2013) 7580–7589.
[20] R. Waksman, R. Erbel, C.D. Mario, J. Bartunek, B.D. Bruyne, F.R. Eberli, P. Erne, M. Haude, M. Horrigan, C. Ilsley, D. Bose, H. Bonnier, J. Koolen, T.F. Luscher, N.J. Weissman, Early- and long-term intravascular ultrasound and angiographic findings after bioabsorbable magnesium stent implantation in human coronary arteries, JACC Cardiovasc. Interv. 2 (2009) 312–320.
[21] M. Haude, R. Erbel, P. Erne, S. Verheye, H. Degen, D. Böse, P. Vermeersch, I. Wijnbergen, N. Weissman, F. Prati, R. Waksman, J. Koolen, Safety and performance of the drug-eluting absorbable metal scaffold (DREAMS) in patients with de-novo coronary lesions: 12 month results of the prospective multicentre, first-in-man BIOSOLVE-I trial, Lancet 381 (2013) 836–844.
[22] L.P. Xu, F. Pan, G.N. Yu, L. Yang, E.L. Zhang, K. Yang, *In vitro* and *in vivo* evaluation of the surface bioactivity of a calcium phosphate coated magnesium alloy, Biomaterials 30 (2009) 1512–1523.
[23] A. Dhanapal, S.R. Boopathy, V. Balasubramanian, Influence of pH value, chloride ion concentration and immersion time on corrosion rate of friction stir welded AZ61A magnesium alloy weldments, J. Alloys Compd. 523 (2012) 49–60.
[24] G.S. Wu, W. Dai, H. Zheng, A.Y. Wang, Improving wear resistance and corrosion resistance of AZ31 magnesium alloy by DLC/AlN/Al coating, Surf. Coat. Technol. 205 (2010) 2067–2073.
[25] B. Zberg, P.J. Uggowitzer, J.F. Loffler, MgZnCa glasses without clinically observable hydrogen evolution for biodegradable implants, Nat. Mater. 8 (2007) 887–891.
[26] F. Witte, V. Kaese, H. Haferkamp, E. Switzer, A. Meyer-Lindenberg, C.J. Wirth, H. Windhagen, *In vivo* corrosion of four magnesium alloys and the associated bone response, Biomaterials 26 (2005) 3557–3563.
[27] R.C. Zeng, L. Sun, Y.F. Zheng, H.Z. Cui, E.H. Han, Corrosion and characterisation of dual phase Mg–Li–Ca alloy in Hank's solution: the influence of microstructural features, Corros. Sci. 79 (2014) 69–82.
[28] Y. Snir, G. Ben-Hamu, D. Eliezer, E. Abramov, Effect of compression deformation on the microstructure and corrosion behavior of magnesium alloys, J. Alloys Compd. 528 (2012) 84–90.
[29] S.H. Ye, Y.S. Jang, Y.H. Yun, V. Shankarraman, J.R. Woolley, Y. Hong, L.J. Gamble, K. Ishihara, W.R. Wagner, Surface modification of a biodegradable magnesium alloy with phosphorylcholine (PC) and sulfobetaine (SB) functional macromolecules for reduced thrombogenicity and acute corrosion resistance, Langmuir 29 (2013) 8320–8327.
[30] K.H. Dong, Y.W. Song, D.Y. Shan, E.H. Han, Corrosion behavior of a self-sealing pore micro-arc oxidation film on AM 60 magnesium alloy, Corros. Sci. (2015), http://dx.doi.org/10.1016/j.corsci.2015.08.004.
[31] I.A. Kartsonakis, A.C. Balaskas, E.P. Koumoulos, C.A. Charitidis, G. Kordas, Evaluation of corrosion resistance of magnesium alloy ZK10 coated with hybrid organic–inorganic film including containers, Corros. Sci. 65 (2012) 481–493.
[32] Y. Zhao, M.I. Jamesh, W.K. Li, G.S. Wu, C.X. Wang, Y.F. Zheng, K.W.K. Yeung, P.K. Chu, Enhanced antimicrobial properties, cytocompatibility, and corrosion resistance of plasma-modified biodegradable magnesium alloys, Acta Biomater. 10 (2014) 544–556.
[33] L. Montanaro, C.R. Arciola, D. Campoccia, M. Cervellati, *In vitro* effects on MG63 osteoblast-like cells following contact with two roughness-differing fluorohydroxyapatite-coated titanium alloys, Biomaterials 23 (2002) 3651–3659.
[34] N. Ostrowski, B. Lee, N. Enick, B. Carlson, S. Kunjukunju, A. Roy, P.N. Kumta, Corrosion protection and improved cytocompatibility of biodegradable polymeric layer-by-layer coatings on AZ31 magnesium alloys, Acta Biomater. 9 (2013) 8704–8713.
[35] G.Y. Liu, S.W. Tang, D.C. Li, J. Hu, Self-adjustment of calcium phosphate coating on micro-arc oxidized magnesium and its influence on the corrosion behaviour in simulated body fluids, Corros. Sci. 79 (2014) 206–214.
[36] M.B. Kannan, Improving the packing density of calcium phosphate coating on a magnesium alloy for enhanced degradation resistance, J. Biomed. Mater. Res. A 101A (2013) 1248–1254.
[37] B.L. Zou, S.Y. Tao, W.Z. Huang, Z.S. Khan, X.Z. Fan, L.J. Gu, Y. Wang, J.Y. Xu, X.L. Cai, H.M. Ma, X.Q. Cao, Synthesis and characterization of *in situ* TiC-TiB_2 composite coatings by reactive plasma spraying on a magnesium alloy, Appl. Surf. Sci. 264 (2013) 879–885.
[38] J. Liang, P. Bala Srinivasan, C. Blawert, W. Dietzel, Comparison of electrochemical corrosion behaviour of MgO and ZrO_2 coatings on AM50 magnesium alloy formed by plasma electrolytic oxidation, Corros. Sci. 51 (2009) 2483–2492.
[39] H.X. Wang, S.K. Guan, X. Wang, C.X. Ren, L.G. Wang, *In vitro* degradation and mechanical integrity of Mg–Zn–Ca alloy coated with Ca-deficient hydroxyapatite by the pulse electrodeposition process, Acta Biomater. 6 (2010) 1743–1748.
[40] S.V. Lamaka, M.F. Montemor, A.F. Galio, M.L. Zheludkevich, C. Trindade, L.F. Dick, M.G.S. Ferreira, Novel hybrid sol–gel coatings for corrosion protection of AZ31B magnesium alloy, Electrochim. Acta 53 (2008) 4773–4783.
[41] G.S. Wu, X.Q. Zeng, G.Y. Li, S.S. Yao, X.M. Wang, Preparation and characterization of ceramic/metal duplex coatings deposited on AZ31 magnesium alloy by multi-magnetron sputtering, Mater. Lett. 60 (2006) 674–678.
[42] L.M. Chang, L.F. Tian, W. Liu, X.Y. Duan, Formation of dicalcium phosphate dihydrate on magnesium alloy by micro-arc oxidation coupled with hydrothermal treatment, Corros. Sci. 72 (2013) 118–124.
[43] G.S. Wu, X.Q. Zeng, G.Y. Yuan, Growth and corrosion of aluminum PVD-coating on AZ31 magnesium alloy, Mater. Lett. 62 (2008) 4325–4327.
[44] X.M. Wang, X.Q. Zeng, G.S. Wu, S.S. Yao, Yttrium ion implantation on the surface properties of magnesium, Appl. Surf. Sci. 253 (2006) 2437–2442.
[45] C.Y. Zheng, S.J. Li, X.J. Tao, Y.L. Hao, R. Yang, L. Zhang, Calcium phosphate coating of Ti–Nb–Zr–Sn titanium alloy, Mater. Sci. Eng. C 27 (2007) 824–831.
[46] Q.Y. Zhang, Y. Leng, R.L. Xin, A comparative study of electrochemical deposition and biomimetic deposition of calcium phosphate on porous titanium, Biomaterials 26 (2005) 2857–2865.
[47] G.S. Wu, X.Q. Zeng, W.B. Ding, X.W. Guo, S.S. Yao, Characterization of ceramic PVD thin films on AZ31 magnesium alloys, Appl. Surf. Sci. 252 (2006) 7422–7429.
[48] Y. Song, S.X. Zhang, J.N. Li, C.L. Zhao, X.N. Zhang, Electrodeposition of Ca–P coatings on biodegradable Mg alloy: *in vitro* biomineralization behavior, Acta Biomater. 6 (2010) 1736–1742.
[49] X.B. Chen, N. Birbilis, T.B. Abbott, Effect of $[Ca^{2+}]$ and $[PO_4^{3-}]$ levels on the formation of calcium phosphate conversion coatings on die-cast magnesium alloy AZ91D, Corros. Sci. 55 (2012) 226–232.
[50] L.P. Xu, A. Yamamoto, Characteristics and cytocompatibility of biodegradable polymer film on magnesium by spin coating, Colloids Surf. B 93 (2012) 67–74.
[51] R. Langer, Drug delivery and targeting, Nature 392 (6679) (1998) 5–10.
[52] J. Gray, B. Luan, Protective coatings on magnesium and its alloys—a critical review, J. Alloys Compd. 336 (2002) 88–113.
[53] S.V. Gnedenkov, S.L. Sinebryukhov, D.V. Mashtalyar, V.S. Egorkin, M.V. Sidorova, A.S. Gnedenkov, Composite polymer-containing protective coatings on magnesium alloy MA8, Corros. Sci. 85 (2014) 52–59.
[54] N.J. Ostrowski, B. Lee, A. Roy, M. Ramanathan, P.N. Kumta, Biodegradable poly(lactide-co-glycolide) coatings on magnesium alloys for orthopedic applications, J. Mater. Sci. Mater. Med. 24 (2013) 85–96.
[55] J.N. Li, P. Cao, X.N. Zhang, S.X. Zhang, Y.H. He, In vitro degradation and cell attachment of a PLGA coated biodegradable Mg–6Zn based alloy, J. Mater. Sci. 45 (22) (2010) 6038–6045.
[56] T. Kokubo, H. Takadama, How useful is SBF in predicting *in vivo* bone bioactivity, Biomaterials 27 (2006) 2907–2915.
[57] C.Z. Yao, Z.C. Wang, S.L. Tay, T.P. Zhu, W. Gao, Effects of Mg on microstructure and corrosion properties of Zn–Mg alloy, J. Alloys Compd. 602 (2014) 101–107.
[58] J.W. Geng, X.Y. Teng, G.R. Zhou, D.G. Zhao, Microstructure transformations in the heat-treated Mg–Zn–Y alloy, J. Alloys Compd. 577 (2013) 498–506.
[59] P. Shi, B. Niu, S.S. E, Y. Chen, Q. Li, Preparation and characterization of PLA coating and PLA/MAO composite coatings on AZ31 magnesium alloy for improvement of corrosion resistance, Surf. Coat. Technol. 262 (2015) 26–32.
[60] Y.H. Li, X.S. Sun, Preparation and characterization of polymer-inorganic nanocomposites by in situ melt polycondensation of L-lactic acid and surface-hydroxylated MgO, Biomacromolecules 11 (2010) 1847–1855.
[61] X.J. Cui, X.Z. Lin, C.H. Liu, R.S. Yang, X.W. Zheng, M. Gong, Fabrication and corrosion resistance of a hydrophobic micro-arc oxidation coating on AZ31 Mg alloy, Corros. Sci. 90 (2015) 402–412.
[62] Y.C. Xin, C.L. Liu, K.F. Huo, G.Y. Tang, X.B. Tian, P.K. Chu, Corrosion behavior of ZrN/Zr coated biomedical AZ91 magnesium alloy, Surf. Coat. Technol. 203 (2009) 2554–2557.
[63] P. Zoltowski, On the electrical capacitance of interfaces exhibiting constant phase element behavior, J. Electroanal. Chem. 443 (1998) 149–154.
[64] S.L. Wu, X.M. Liu, T. Hu, J. Jiang, P.K. Chu, K.W.K. Yeung, C.Y. Chung, C.L. Chu, Z.S. Xu, W.W. Lu, K.M.C. Cheung, K.D.K. Luk, Electrochemical stability of orthopedic porous NiTi shape memory alloys treated by different surface modification techniques, J. Electrochem. Soc. 156 (2009) C187–C194.
[65] S.T. Liu, G.H. Nancollas, The crystallization of magnesium hydroxide, Desalination 12 (1973) 75–84.
[66] Y.H. Wu, N. Li, Y. Cheng, Y.F. Zheng, Y. Han, In vitro study on biodegradable AZ31 magnesium alloy fibers reinforced PLGA composite, J. Mater. Sci. Technol. 29 (6) (2013) 545–550.